

# PREDICTIONS BASED ON PIXEL DATA: INSIGHTS FROM PDES AND FINITE DIFFERENCES

ELENA CELLEDONI, JAMES JACKAMAN, DAVIDE MURARI, AND BRYNJULF OWREN

**ABSTRACT.** Neural networks are the state-of-the-art for many approximation tasks in high-dimensional spaces, as supported by an abundance of experimental evidence. However, we still need a solid theoretical understanding of what they can approximate and, more importantly, at what cost and accuracy. One network architecture of practical use, especially for approximation tasks involving images, is convolutional (residual) networks. However, due to the locality of the linear operators involved in these networks, their analysis is more complicated than for generic fully connected neural networks. This paper focuses on sequence approximation tasks, where a matrix or a higher-order tensor represents each observation. We show that when approximating sequences arising from space-time discretisations of PDEs we may use relatively small networks. We constructively derive these results by exploiting connections between discrete convolution and finite difference operators. Throughout, we design our network architecture to, while having guarantees, be similar to those typically adopted in practice for sequence approximation tasks. Our theoretical results are supported by numerical experiments which simulate linear advection, the heat equation, and the Fisher equation. The implementation used is available at the repository associated to the paper [30].

## 1. INTRODUCTION

When endeavouring to understand the world around us, continuum modelling through partial differential equations (*PDEs*) [20, 52] has proven a fundamental tool for a plethora of applications. Indeed, any process one may envision is expressible as a differential equation through an appropriate simplification, be the focus fluid flows [55, e.g.], mathematical biology [19], chemical engineering [24], or anything in-between. In practice, such models are typically solved approximately utilising the rich toolbox established by the fields of numerical analysis and scientific computing. Popular techniques include finite difference methods [36], finite element methods [8], and spectral methods [7], and have proven excellent tools for simulating PDEs. However, they are subject to two limitations: Firstly, one must be careful to preserve the underlying PDE physics when simulating dynamics over long time (leading to the field of geometric numerical integration [27]). Secondly, the accuracy of the model in practice is restricted by virtue of the PDE model, that is to say a PDE can only describe behaviours which (on some level) are understood well enough to be encoded. They can never truly capture the underlying molecular dynamics, and are limited in their ability to incorporate observed data.

Over the past decade(s) there has been an explosion of research interest in artificial intelligence and machine learning, with applications in almost every area imaginable, from self-driving cars to weather forecasting [6, 48]. One increasingly popular application for machine learning is in the approximation of PDEs. Indeed, this has led to the development of several new technologies, such as physics informed neural networks (*PINNs*) [16, 45]. Such models are powerful tools for approximating PDE dynamics as they typically build some level of PDE structure into the network, and may be exploited to both solve PDEs, and to identify an underlying PDE. Outside of PINNs, significant progress has also been made in solving the inverse problem [5, 47, 59]. While PINNs have proven effective for solving given (families of) PDEs, they have not been shown to be efficient solution methods when using real data.

An important step towards incorporating physical knowledge into more standard networks is to construct neural networks which capture the structure of families of PDEs but are trained on data which does not necessarily arise from a PDE. Progress has been made in this direction in [37] where a methodology for equating carefully structured convolutional layers to finite difference quotients is developed. Indeed, by ensuring the network contains a variety of finite difference quotients one may train a neural network which accurately simulates dynamics for remarkably large classes of PDEs based on simulated data, although the network itself is highly restricted. One crucial observation we make in this work (and, to a certain extent, in [3]) is that *by imposing no restrictions on the convolutional layers one may build a convolutional neural*

network which contains within it a large class of finite difference discretisations of PDEs. Specifically, here we require particular choices of activation functions and design the network with sufficiently wide convolutional layers. We shall exploit this connection in our analysis in section 3. An additional benefit of working with unrestricted networks is they contain *more* than discrete solutions to PDEs, and as such are more amenable to real world datasets. We note that the connection between convolutions and finite differences has also been used in [17, 37, 42, 53].

To incorporate physics into the network, one may also work directly with properties of the PDE (such as conserved quantities) [4, 11, 15, 31, 56, 57, 60]. In addition to incorporating physics into the network such structures often afford stability when training networks, which we exploit in our numerical experiments when the underlying PDE is not dissipative.

In this contribution, we focus on simulating space-time dynamics with PDEs in mind. In particular, we restrict our study to two-dimensional space (visualising our spatial data as a matrix in  $(x, y)$  space) and take discrete “snapshots” in time. This data structure may be interpreted as a video, and with this in mind we draw inspiration from existing (convolutional) techniques for neural networks [21, 38, 39, 58]. An example of a PDE we will consider is the Fisher equation, a nonlinear reaction diffusion equation. We anticipate the results in figure 1, with details found in subsection 4.3.

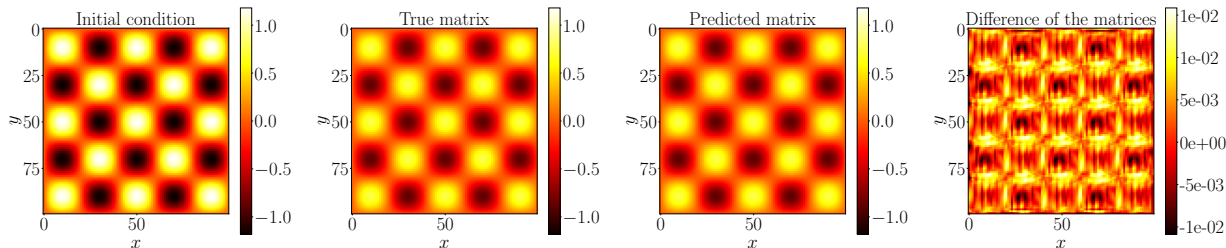


FIGURE 1. Visual representation of the prediction provided by the neural network we consider for one specific test initial condition, and snapshots coming from the space-time discretisation of the reaction diffusion equation (40). The parameters of the network and of the PDE can be found respectively in subsection 4.3 and appendix A. From the left we have the initial condition, the true space discretisation of the solution at time  $40\delta t$ , the network prediction, and the difference between the last two matrices.

In our simulations, we follow a method-of-lines type approach [49, 50]. Temporally, we use a numerical integrator to step forward in time, where the step forward depends on a flow map approximated by a convolutional neural network (*CNN*) which depends on the spatial matrix at fixed times. Similar ideas have been successfully applied for ODEs in [9, 13, 18, 26].

Crucially, we will prove that, if our true dynamics are that of a linear PDE, a relatively standard CNN can converge optimally in time (under the assumption that the spatial information is sufficiently well resolved). We will illustrate this result for a class of nonlinear PDEs and discuss the difficulties with extending this methodology to more general nonlinearities.

The remainder of this paper is structured as follows: In section 2, we discuss residual neural networks for dynamical systems introducing the fundamental tools we use to build our method and how it interacts with neural networks. In section 3, we restrict our focus to approximating PDE solutions and conduct analysis of the method. In section 4, we conduct numerical experiments verifying the good dynamical behaviour of the proposed methods. In section 5, we make concluding remarks and finally, for completeness, in appendix A we describe our data generation procedure.

## 2. RESIDUAL NEURAL NETWORKS INSPIRED BY DYNAMICAL SYSTEMS

Neural networks are defined through compositions of parametric maps. The parameters are then optimised so that the resulting function can accurately solve a specific task. The applications where they have been

successfully applied typically involve approximations in high-dimensional spaces. In this work, we focus on residual neural networks (*ResNets*). This family of networks is defined by composing functions of the form

$$x \mapsto x + G_\theta(x, \theta_i), \quad \theta_i \in \mathcal{P}, i = 1, \dots, L, \quad (1)$$

where  $\mathcal{P}$  is the space of admissible parameters,  $G_\theta$  is a fixed function with outputs in a linear space  $V$ ,  $x \in V$ , and  $L$  is the number of layers. As already pointed out in many previous works (see, e.g., [9, 13, 18, 26]), one can introduce a step size  $\delta t > 0$  and consider

$$x + \delta t \frac{1}{\delta t} G_\theta(x, \theta_i) =: x + \delta t F_\theta(x, \theta_i),$$

which is an explicit Euler step of size  $\delta t$  (from time  $t_i$  to  $t_{i+1}$ ) approximating the solution of the ordinary differential equation (*ODE*)

$$\begin{cases} \dot{x}(t) = F_\theta(x(t), \theta(t)) \\ x(t_i) = x. \end{cases}$$

This connection opens up many possibilities in the design and analysis of both new and established ResNets (see, e.g., [11, 26]). More precisely, one can extend the classical structure of a ResNet in (1) by suitably designing the vector field  $F_\theta$  and replacing the explicit Euler step with any numerical method of choice.

We will now present the framework we adopt in this paper and look for possible and reasonable extensions of (1) in this context. We wish to approximate the temporal updates characterising a sequence of images. Throughout, we restrict our study to grey-scale images. That is to say, our spatial information may be directly represented by matrices. We formalise the problem as follows:

**Problem:** Let  $\{(U_i^0, U_i^1, \dots, U_i^M)\}_{i=1}^N$  be a set of  $N$  observed sequences each containing  $M + 1$  temporal snapshots. To be concise, we write  $U_i^j \in \mathbb{R}^{r \times s}$ , where the observation times are  $t_j$ ,  $j = 0, \dots, M$ . When referring to a single sequence, we suppress the subscript  $i$  and write  $\{U^j\}_{j=0, \dots, M}$  to simplify exposition. Suppose there is a map  $\Phi$  such that

$$[U_i^{k-j+1}, \dots, U_i^k] := \Phi([U_i^{k-j}, \dots, U_i^{k-1}]) \quad i = 1, \dots, N, j \leq k \leq M - 1, \quad (2)$$

then our goal is to obtain an accurate approximation of  $\Phi$  which can reproduce unseen time sequences generated by the same dynamics (i.e., on a test set).

Throughout the paper, we denote a tensor of order 3 as

$$\mathbf{X} = [X_1, \dots, X_j] \in \mathbb{R}^{j \times r \times s}, \quad (3)$$

where  $X_i \in \mathbb{R}^{r \times s}$ . We will also consider 4-th order tensors, which we write as

$$\mathbf{x} = [\mathbf{X}_1, \dots, \mathbf{X}_k] \in \mathbb{R}^{k \times j \times r \times s} \quad (4)$$

where  $\mathbf{X}_i \in \mathbb{R}^{j \times r \times s}$ . We may access lower dimensional tensors through the standard index notation

$$\mathbb{R}^{k \times j \times r \times s} \ni \mathbf{x} = [\mathbf{X}_1, \dots, \mathbf{X}_k] \implies \mathbf{x}[h] = \mathbf{X}_h, \quad (5)$$

$$\mathbb{R}^{j \times r \times s} \ni \mathbf{X}_h = [X_{h1}, \dots, X_{hj}] \implies \mathbf{x}[h, k] = X_{hk} \in \mathbb{R}^{r \times s}. \quad (6)$$

For the case  $\mathbf{X} = [X_1] \in \mathbb{R}^{1 \times r \times s}$ , we will often contract the first dimensionality and refer to it as the matrix  $X_1 \in \mathbb{R}^{r \times s}$ . Furthermore, we adopt the notation  $\Phi_F^t$  to denote the exact flow, at time  $t$ , of the vector field  $F$ , and generally  $\Psi_F^{\delta t}$  to denote one of its numerical approximations at time  $\delta t$ .

The numerical experiments that we report are for time sequences arising from space-time discretisations of PDE solutions and, in that case, the data may be interpreted as

$$(U^j)_{hk} \approx u(t_j, x_h, y_k), \quad \text{where } (U^0)_{hk} = u(0, x_h, y_k).$$

In the above expression  $u : \mathbb{R} \times \mathbb{R}^2 \rightarrow \mathbb{R}$  is the solution of a PDE,  $(x_h, y_k)$  is a spatial grid point, and  $t_j$  is a temporal discretisation point.

Since our data will be driven by a dynamical system we choose to approximate the updating map  $\Phi$  with ResNets. In practice, we follow three steps to approximate  $\Phi$ .

- (1) Define an approximate vector field  $F_\theta$  that can provide both a qualitatively and quantitatively accurate approximation for the problem of interest.
- (2) Choose a one-step numerical method that is compatible with the dynamics to be approximated.

- (3) Choose a suitable loss function and minimise the discrepancy between the model predictions and the training data.

**2.1. Characterisation of the vector field.** Let us first focus on the first of these three steps, the selection of the vector field  $F_\theta$ . This characterisation is theoretically justified in section 3. To define the vector field  $F_\theta$  we start from the approach presented in [3,38], and propose modifications aiming to capture multiplicative interactions typical of physical systems. This has been observed in [37], but our approach differs in that our architecture is more compatible with architectures typically used for CNNs. Our primary goal is to understand the theory behind which types of PDEs can be well represented and approximated using networks similar to those in [3,38]. We present the derivation of such results in section 3, which utilises the connection between discrete convolution and finite difference operators. We show that these representation results can be theoretically obtained with small networks, as anticipated in algorithm 1. In such an algorithm, we denote the different convolutional operators defining the network as  $\text{Conv}_1, \dots, \text{Conv}_5$ . Furthermore, we highlight that these networks can be contained as subnetworks of larger ones that are then used in practice to approximate PDE dynamics.

---

**Algorithm 1** Prototypical network proposed in the manuscript

---

- 1: **Input:**  $U \in \mathbb{R}^{r \times s}$
  - 2:  $L \leftarrow \text{Conv}_2\left(\max(0, \text{Conv}_1(U))\right)$
  - 3:  $Q \leftarrow \text{Conv}_4\left(\max(0, \text{Conv}_3(L))^2\right)$
  - 4:  $F_\theta(U) \leftarrow Q + \text{Conv}_5(L)$
  - 5: **return**  $F_\theta(U)$
- 

**2.2. Numerical time integrator.** We now move on to the second step, namely the choice of the numerical integrator defining the network. We first present the general case where we ask  $1 \leq j \leq M$ , then we specialise it to the most typical situation with  $j = 1$ . For a generic  $j$ , one can consider a parametrised differential equation defined on the space of 3-dimensional tensors of shape  $j \times r \times s$ . Let  $F_\theta$  be a parametrised vector field on  $\mathbb{R}^{j \times r \times s}$ . With this in mind, we define the tensor  $\mathbf{X}(t) \in \mathbb{R}^{j \times r \times s}$  such that

$$\begin{cases} \dot{\mathbf{X}}(t) = F_\theta(\mathbf{X}(t)) \\ \mathbf{X}(0) = \mathbf{U}^0 = [U^0, \dots, U^{j-1}] \in \mathbb{R}^{j \times r \times s}. \end{cases}$$

In order to define a ResNet one can choose any numerical method  $\Psi_{F_\theta}^{\delta t} : \mathbb{R}^{j \times r \times s} \rightarrow \mathbb{R}^{j \times r \times s}$ , apply it to the vector field  $F_\theta$ , and define the neural network  $\mathcal{N}_\theta : \mathbb{R}^{j \times r \times s} \rightarrow \mathbb{R}^{j \times r \times s}$  as

$$\mathcal{N}_\theta(\mathbf{U}^0) = \hat{\mathbf{U}}^1 := \Psi_{F_\theta}^{\delta t}(\mathbf{U}^0) \approx \mathbf{X}(\delta t).$$

In this case we define  $\hat{\mathbf{U}}^1 := [\hat{U}^1, \dots, \hat{U}^j]$  that aims to provide an accurate approximation of  $[U^1, \dots, U^j]$ , a tensor containing the correct update correspondent to the  $j$  input snapshots. Given this network description, we now focus on the case  $j = 1$ . Here the dynamics reduce to the matrix differential equation

$$\begin{cases} \dot{X}(t) = F_\theta(X(t)) \\ X(0) = U^0, \end{cases} \quad (7)$$

where  $F_\theta$  is a vector field on  $\mathbb{R}^{r \times s}$ . The network will then be given by

$$\mathcal{N}_\theta(U^0) := \Psi_{F_\theta}^{\delta t}(U^0),$$

for some numerical method  $\Psi_{F_\theta}^{\delta t} : \mathbb{R}^{r \times s} \rightarrow \mathbb{R}^{r \times s}$  applied to  $F_\theta$ . In our numerical experiments, the map  $\Psi_{F_\theta}^{\delta t}$  will generally be defined by composing  $s$  substeps of a numerical method  $\varphi_{F_\theta}^{\delta t/s}$  with time step  $\delta t/s$ . Thus the network will be expressed as

$$\mathcal{N}_\theta(U^0) = \Psi_{F_\theta}^{\delta t}(U^0) = \underbrace{\varphi_{F_\theta}^{\delta t/s} \circ \dots \circ \varphi_{F_\theta}^{\delta t/s}}_{s \text{ times}}(U^0).$$

We will highlight with the numerical experiments that if one desires some kind of mathematical guarantee on the predictions or wishes to reproduce some physical behaviour, there is quite a lot of freedom in the design of the numerical method. This is one of the main advantages of detaching the design of the vector field  $F_\theta$  from the choice of the numerical method in the process of assembling the neural network. While not integral to our main result in section 3, we shall explore norm-preserving neural networks. Indeed, if our data preserves the spatial matrix norm over time this is a property we wish to exploit through our choice of integrator and affords a degree of stability to a neural network. Experimentally, we shall consider one such problem in linear advection, but our study here eludes to conservation of invariants for more general Hamiltonian PDEs. Here, we rely on projection methods (see, [27, Section 4.4] and [32]) in order to preserve a desired property, for example, the norm of the solution. In particular, in section 4 we report numerical experiments based on the following two integrators:

$$\begin{aligned}\Psi_{1,F}^{\delta t}(X) &= X + \delta t F(X), & \text{Explicit Euler,} \\ \Psi_{2,F}^{\delta t}(X) &= n_{\delta t}(X)(X + \delta t F(X)), & \text{Norm preserving projected Euler.}\end{aligned}$$

We remark that

$$n_{\delta t}(X) = \frac{\|X\|}{\|X + \delta t F(X)\|},$$

where  $\|X\| = \text{trace}(X^T X)^{\frac{1}{2}}$  is the Frobenius norm of  $X$ , which enforces that  $\|\Psi_{2,F}^{\delta t}(X)\| = \|X\|$ . We adopt the same notation for this norm from now on. Another appealing structure to exploit, which we plan to investigate more in future work, is the inherent low-rank structure typical for some datasets (see [2,12,34,35]). We now present two results that motivate our choices of numerical methods, and also their use in other (more general) contexts.

**Lemma 2.1** (See [27]). Let  $F$  be a norm-preserving vector field on  $\mathbb{R}^{r \times s}$ , i.e.,  $X, \Phi_F^t(X) \in \mathbb{R}^{r \times s}$  with  $\|\Phi_F^t(X)\| = \|X\|$  for all  $t \geq 0$ . Then the numerical method  $\Psi_{2,F}^{\delta t}$  is a first-order accurate approximation of the exact flow.

*Proof.* We first notice that

$$\begin{aligned}\Psi_{1,F}^{\delta t}(X) &= \Phi_F^{\delta t}(X) + \mathcal{O}(\delta t^2) \\ \implies \frac{\|X\|}{\|\Psi_{1,F}^{\delta t}(X)\|} \Psi_{1,F}^{\delta t}(X) &= \frac{\|X\|}{\|\Psi_{1,F}^{\delta t}(X)\|} \Phi_F^{\delta t}(X) + \frac{\|X\|}{\|\Psi_{1,F}^{\delta t}(X)\|} \mathcal{O}(\delta t^2).\end{aligned}$$

Further, by classical properties of numerical methods (see, e.g., [27, page 110]),  $\|\Psi_{1,F}^{\delta t}(X)\| = \|X\| + \mathcal{O}(\delta t^2)$  since the constraint violation is of the order of the local error of the method. Thus

$$\frac{\|X\|}{\|\Psi_{1,F}^{\delta t}(X)\|} = \frac{\|X\|}{\|X\| + \mathcal{O}(\delta t^2)} = \|X\| \frac{1}{\|X\|(1 - \mathcal{O}(\delta t^2))} = 1 + \mathcal{O}(\delta t^2).$$

As a consequence, we see that

$$\Psi_{2,F}^{\delta t}(X) = \frac{\|X\|}{\|\Psi_{1,F}^{\delta t}(X)\|} \Psi_{1,F}^{\delta t}(X) = \Psi_{1,F}^{\delta t}(X) + \mathcal{O}(\delta t^2) = \Phi_F^{\delta t}(X) + \mathcal{O}(\delta t^2),$$

hence the order of the method is preserved.  $\square$

This result extends to any numerical method of order  $r$ , since the projection we apply does not change the order of the underlying method. However, if  $F$  is not preserving the norm, the result above no longer applies. Following a similar approach to [32] we now focus on the more general case where  $F$  is an arbitrary vector field. The result is presented for a generic submanifold  $\mathcal{M} \subset \mathbb{R}^{r \times s}$ , but one can think to the specific case  $\mathcal{M} = \{X \in \mathbb{R}^{r \times s} : \|X\| = c\}$  of matrices with a constant norm  $c$ .

**Lemma 2.2.** Let  $F$  be a smooth vector field on  $\mathbb{R}^{r \times s}$ ,  $\mathcal{M} \subset \mathbb{R}^{r \times s}$  be a smooth submanifold of  $\mathbb{R}^{r \times s}$ , and  $P_{T_X \mathcal{M}} : \mathbb{R}^{r \times s} \rightarrow T_X \mathcal{M}$  be the orthogonal projection onto the tangent space at  $X \in \mathcal{M}$  of  $\mathcal{M}$  (with respect to the Euclidean metric of the ambient space  $\mathbb{R}^{r \times s}$ ). Then, the projection method

$$X \mapsto \Pi_{\mathcal{M}}(\Psi_{1,F}^{\delta t}(X))$$

satisfies  $\|\Pi_{\mathcal{M}}(\Psi_{1,F}^{\delta t}(X)) - \Phi_{F^{\parallel}}^{\delta t}(X)\| \leq \bar{c}\delta t(\varepsilon + \delta t)$  where

$$F(X) = P_{T_X\mathcal{M}}F(X) + (I - P_{T_X\mathcal{M}})F(X) := F^{\parallel}(X) + F^{\perp}(X), \quad \|F^{\perp}(X)\| \leq \varepsilon,$$

and  $\Pi_{\mathcal{M}} : \mathbb{R}^{r \times s} \rightarrow \mathcal{M}$  is the orthogonal projection on the manifold.

*Proof.* We have

$$\begin{aligned} \Psi_{1,F}^{\delta t}(X) &= X + \delta t F(X) = X + \delta t F^{\parallel}(X) + \delta t F^{\perp}(X), \\ &= \Phi_{F^{\parallel}}^{\delta t}(X) + \mathcal{O}(\delta t^2) + \delta t F^{\perp}(X). \end{aligned}$$

This allows getting

$$\begin{aligned} \|\Pi_{\mathcal{M}}(\Psi_{1,F}^{\delta t}(X)) - \Phi_{F^{\parallel}}^{\delta t}(X)\| &= \|\Pi_{\mathcal{M}}(\Psi_{1,F}^{\delta t}(X)) - \Psi_{1,F}^{\delta t}(X) + \mathcal{O}(\delta t^2) + \delta t F^{\perp}(X)\| \\ &\leq \|\Pi_{\mathcal{M}}(\Psi_{1,F}^{\delta t}(X)) - \Psi_{1,F}^{\delta t}(X)\| + c\delta t^2 + \delta t\varepsilon \\ &\leq_{(\#)} \|\Phi_{F^{\parallel}}^{\delta t}(X) - \Psi_{1,F}^{\delta t}(X)\| + c\delta t^2 + \delta t\varepsilon \\ &= \|\mathcal{O}(\delta t^2) + \delta t F^{\perp}(X)\| + c\delta t^2 + \delta t\varepsilon \\ &\leq 2c\delta t(\delta t + \varepsilon). \end{aligned}$$

We remark that inequality (#) comes from the definition of orthogonal projection, since  $F^{\parallel} \in \mathfrak{X}(\mathcal{M})$  and hence  $\Phi_{F^{\parallel}}^{\delta t}(X) \in \mathcal{M}$ . Furthermore,  $c$  is a constant independent on  $\delta t$ .  $\square$

This lemma guarantees that the projection method  $\Psi_{2,F}^{\delta t}$  provides a consistent and convergent approximation of  $\Phi_{F^{\parallel}}^{\delta t}$  only if  $\varepsilon < \bar{c}\delta t$  for some constant  $\bar{c}$  independent on  $\delta t$ . In the experiments, we will not constrain the vector field  $F$  to be tangent to a non-linear submanifold  $\mathcal{M} \subset \mathbb{R}^{r \times s}$ , as supposed in lemma 3.1. The analysis we present in the next section focuses on generic order  $r$  approximations of the exact flow  $\Phi_F^{\delta t}$ . In practice, we will observe in section 4, that the approximations we obtain with  $\Psi_{2,F}^{\delta t}$  are more reliable and accurate in the case of the linear transport problem. In light of lemma 2.2, a possible motivation of these results is that the norm of the perpendicular component of the learned vector fields can be controlled by a small  $\varepsilon$ , thus maintaining the approximation properties of the complete vector field  $X$  while still preserving  $\mathcal{M}$ . However, this requires additional theoretical and experimental study. Other options are available to generate predictions constrained to a submanifold  $\mathcal{M} \subset \mathbb{R}^{r \times s}$ , for example using suitable implicit numerical integrators. Due to the dimensionality of the problems we consider, we restrict ourselves to explicit integrators here as implicit integrators involve solving non-linear systems to obtain the predictions from a trained model.

**2.3. Optimisation problem to solve.** We conclude this section with the third step, reporting the loss function that is optimised in order to find the final approximate function  $\mathcal{N}_{\theta}$ . We do so in the general case of  $1 \leq j \leq M$ . In the numerical experiments reported in section 4 we focus on the regression loss function given by

$$\begin{aligned} \text{Loss}(\theta) &:= \frac{1}{B \cdot M} \sum_{i=1}^B \sum_{m=j}^M \left\| \mathcal{N}_{\theta}([\hat{U}_i^{m-j}, \dots, \hat{U}_i^{m-1}]) - \Phi([U_i^{m-j}, \dots, U_i^{m-1}]) \right\|^2 = \\ &= \frac{1}{B \cdot M} \sum_{i=1}^B \sum_{m=j}^M \left\| \mathcal{N}_{\theta}([\hat{U}_i^{m-j}, \dots, \hat{U}_i^{m-1}]) - [U_i^{m-j+1}, \dots, U_i^m] \right\|^2, \end{aligned}$$

where  $B$  is the size of one training batch, and we update the  $\hat{U}_i^j$  as follows

$$\begin{aligned} [\hat{U}_i^0, \dots, \hat{U}_i^{j-1}] &= [U_i^0, \dots, U_i^{j-1}], \\ [\hat{U}_i^{m-j+1}, \dots, \hat{U}_i^m] &= \mathcal{N}_{\theta}([\hat{U}_i^{m-j}, \dots, \hat{U}_i^{m-1}]), \quad m \geq j. \end{aligned}$$

For clarity, we remark that in the case  $j = 1$  this reduces to the simpler relation

$$\begin{aligned} \hat{U}_i^0 &= U_i^0, \\ \hat{U}_i^{j+1} &= \mathcal{N}_{\theta}(\hat{U}_i^j). \end{aligned}$$

The set  $\{U_i^j\}_{i,j}$  collects the training data points, while  $\{\hat{U}_i^j\}_{i,j}$  the network predictions. This approach is often called recurrent training in the literature (see, e.g., [10, 14]) and aims to control the accumulation of errors due to the iterative application of the neural network to make predictions.

### 3. APPROXIMATING PDE SOLUTIONS

In this section we present a theoretical analysis of the approximation properties of some neural networks when temporal sequences arise from solutions of PDEs. Let us restrict our focus to seeking solutions of the form  $u = u(t, x, y)$  for  $u$  scalar which satisfy PDEs of the form

$$\partial_t u = \mathcal{L}u + \sum_{i=1}^n \beta_i \partial_{\alpha_{i1}} u \cdot \dots \cdot \partial_{\alpha_{im_i}} u, \quad \beta_i \in \mathbb{R}, \quad \alpha_{ij} \in \mathbb{N}^2, \quad (8)$$

where  $\partial_\alpha u := \frac{\partial^{|\alpha|} u}{\partial x^{\alpha_1} \partial y^{\alpha_2}}$ ,  $\alpha = (\alpha_1, \alpha_2) \in \mathbb{N}^2$  is a multi-index and  $|\alpha| = \alpha_1 + \alpha_2$ . Further, the operator  $\mathcal{L}$  is a linear differential operator. The proofs we present focus on second-order PDEs defined on the domain  $\Omega := [0, 1]^2$ . The extension to more general domains and higher-order PDEs can be achieved following similar principles but requires significantly more exposition.

Let  $(x, y) \in \Omega$ ,  $t \in [0, T]$ , then we partition our space-time domain with

$$0 = t_0 < t_1 < \dots < t_M = T, \quad 0 = x_1 < \dots < x_p = 1, \quad 0 = y_1 < \dots < y_p = 1,$$

where we assume all points are equidistributed within their own dimension (to simplify notion). Given this partition we define the step sizes

$$\delta t = t_{j+1} - t_j, \quad \delta x = x_{h+1} - x_h, \quad \delta y = y_{k+1} - y_k.$$

In the experiments we always set  $\delta x = \delta y$  and hence, from now on, we suppose  $\delta y = \delta x$  and only mention  $\delta x$  in the derivations. We restrict our focus to evolutionary PDEs, that is we study PDE dynamics which may be approximated given some space-time observations of the dynamics, which we refer to as snapshots. This falls within the same framework introduced in the previous section, however to make this derivation self-contained we briefly recall and adapt the notation. Consider the dataset  $\{(U_i^0, U_i^1, \dots, U_i^M)\}_{i=1}^N$ ,  $U_i^j \in \mathbb{R}^{p \times p}$ , where

$$(U_i^0)_{hk} = u_i(0, x_h, y_k) \quad (9)$$

$$(U_i^j)_{hk} = u_i(t_j, x_h, y_k) + \varepsilon_i^j(x_h, y_k), \quad i = 1, \dots, N, \quad j = 1, \dots, M, \quad (h, k) \in \{1, \dots, p\}^2, \quad (10)$$

$N$  corresponds to the number of samples,  $p \times p$  the dimension of the spatial snapshot,  $M$  the number of snapshots, and  $\varepsilon_i^j$  the measurement error at  $t = t_j$  accounting for the fact that we generally do not have access to the analytical solution  $u$ . Throughout the remainder of this section, similarly to section 2, we suppress the batch index and write  $U_i^j = U^j$  for clarity of exposition. Our goal is to find a map  $\mathcal{N}_\theta$  which accurately approximates the function

$$U^j \mapsto \Phi(U^j) = U^{j+1} + \varepsilon^{j+1}, \quad j = 0, \dots, M-1.$$

To analyse how well such a map can be approximated, follow the philosophy of the method of lines (see, e.g., [49, 50]). More precisely, we assume the PDE (8) is discretised in space with a second-order accurate approximation and obtain a matrix ODE of the form

$$\dot{U}(t) = L * U(t) + \sum_{i=1}^n \beta_i [(D_{i1} * U(t)) \odot \dots \odot (D_{im_i} * U(t))] = X(U(t)) \in \mathbb{R}^{p \times p} \quad (11)$$

where  $\odot$  is the Hadamard product, i.e. the entry-wise product, and  $D_{ij} * U$  is the discrete convolution of the kernel  $D_{ij}$  with the matrix  $U$ . We will prove in section 3.2.1 that it is possible to have a consistent space discretisation of the PDE of the form (11), however we first present how the reasoning proceeds and how to quantify the approximation error in time through a sequence of snapshots.

**3.1. Splitting of the approximation errors.** Let  $\Phi_X^{\delta t}$  be the exact flow map of the ODE (11), and consider the semi-discretised PDE (11). Accounting for the spatial discretisation that we suppose is second order accurate, we have

$$\|U^{j+1} - \Phi_X^{\delta t}(U^j)\| = \mathcal{O}(\delta x^2) + \|\varepsilon^{j+1}\|.$$

If we think about the snapshots  $U^j$  as grey-scale images, we can say that the higher the resolution of the image, the smaller  $\delta x$  and hence the higher the accuracy of our spatial discretisation. This spatial error is uncontrollable and depends on the quality of the available snapshots. Therefore we focus on the approximation of the unknown ODE defined in (11). More precisely, we will see how well we can approximate the flow map  $\Phi_X^{\delta t}$  of  $X$  given a parametric set of functions  $\mathcal{F} = \{F_\theta : \mathbb{R}^{p \times p} \rightarrow \mathbb{R}^{p \times p} : \theta \in \mathcal{P}\}$  for a set of admissible parameters  $\mathcal{P}$  inducing a mapping of the form

$$U \mapsto \Psi_{F_\theta}^{\delta t}(U), \quad F_\theta \in \mathcal{F}.$$

Recall, as introduced in section 2, that map  $\Psi_{F_\theta}^{\delta t}$  is a one-step numerical method applied to the ODE

$$\begin{cases} \dot{U}(t) = F_\theta(U(t)) \\ U(0) = U^0. \end{cases}$$

Through splitting the local error, starting from position  $U^j$ , we may write

$$\|U^{j+1} - \Psi_{F_\theta}^{\delta t}(U^j)\| \tag{12}$$

$$= \|\varepsilon^j + \mathcal{O}(\delta x^2) + \Phi_X^{\delta t}(U^j) - \Psi_{F_\theta}^{\delta t}(U^j)\| \tag{13}$$

$$\leq \|\varepsilon^j\| + \mathcal{O}(\delta x^2) + \|\Phi_X^{\delta t}(U^j) - \Psi_{F_\theta}^{\delta t}(U^j)\| \tag{14}$$

$$\leq \underbrace{\|\varepsilon^j\|}_{\text{measurement error}} + \underbrace{\mathcal{O}(\delta x^2)}_{\text{spatial error}} + \underbrace{\|\Phi_X^{\delta t}(U^j) - \Psi_X^{\delta t}(U^j)\|}_{\text{classical error estimate}} + \underbrace{\|\Psi_X^{\delta t}(U^j) - \Psi_{F_\theta}^{\delta t}(U^j)\|}_{\text{neural network approximation}}. \tag{15}$$

The classical term of the estimate is so in the sense that it only depends on the local truncation error of the numerical method  $\Psi^{\delta t}$ . Indeed, this term is  $\mathcal{O}(\delta t^{r+1})$  if  $\Psi^{\delta t}$  is a method of order  $r$ , allowing us to write

$$\Psi^{\delta t}(U) = \Phi^{\delta t}(U) + \mathcal{O}(\delta t^{r+1})$$

telling us that

$$\|U^{j+1} - \Psi_{F_\theta}^{\delta t}(U^j)\| \leq \mathcal{O}(\delta x^2) + \mathcal{O}(\delta t^{r+1}) + \|\varepsilon^j\| + \|\Psi_X^{\delta t}(U^j) - \Psi_{F_\theta}^{\delta t}(U^j)\|.$$

We now introduce an assumption that is not too restrictive in practice. Suppose there is a constant  $c > 0$  such that the solution  $U(t)$  of (11) satisfies

$$\|U(t)\| \leq c \quad \forall t \in [0, T].$$

This allows us to control the Lipschitz constant of the vector field in (8), which otherwise would be a non-Lipschitz function. To control the second term on the right-hand side of (15) we first rewrite the numerical flow  $\Psi_X^{\delta t}(U)$  in terms of the exact flow  $\Phi_X^{\delta t}$ . In particular, we utilise

$$\Psi_X^{\delta t}(U) = \Phi_X^{\delta t}(U) + \mathcal{O}(\delta t^{r+1}), \quad \Psi_{F_\theta}^{\delta t}(U) = \Phi_{F_\theta}^{\delta t}(U) + \mathcal{O}(\delta t^{r+1})$$

allowing us to express

$$\|\Psi_X^{\delta t}(U_i^j) - \Psi_{F_\theta}^{\delta t}(U_i^j)\| \leq \mathcal{O}(\delta t^{r+1}) + \|\Phi_X^{\delta t}(U_i^j) - \Phi_{F_\theta}^{\delta t}(U_i^j)\|. \tag{16}$$



We now bound the second term with Gronwall’s inequality, by working with the integral representation of the flow map:

$$\begin{aligned}
\|\Phi_X^{\delta t}(U) - \Phi_{F_\theta}^{\delta t}(U)\| &\leq \int_0^{\delta t} \|X(\Phi_X^s(U)) - F_\theta(\Phi_{F_\theta}^s(U))\| \, ds \\
&= \int_0^{\delta t} \|X(\Phi_X^s(U)) - X(\Phi_{F_\theta}^s(U)) + X(\Phi_{F_\theta}^s(U)) - F_\theta(\Phi_{F_\theta}^s(U))\| \, ds \\
&\leq \text{Lip}(X) \int_0^{\delta t} \|\Phi_X^s(U) - \Phi_{F_\theta}^s(U)\| \, ds + \delta t \sup_{\|U\| \leq c} \|F_\theta(U) - X(U)\| \\
&\implies \|\Phi_X^{\delta t}(U) - \Phi_{F_\theta}^{\delta t}(U)\| \leq \delta t \exp(\text{Lip}(X)\delta t) \sup_{\|U\| \leq c} \|F_\theta(U) - X(U)\|.
\end{aligned}$$

Thus, to control from above such a quantity we need to understand the approximation properties of  $\mathcal{F}$ . In particular, we want to quantify how much complexity  $\mathcal{F}$  requires in order for

$$\sup_{\|U\| \leq c} \|F_\theta(U) - X(U)\| < c\delta t^k \tag{17}$$

for some  $k \geq 1$ . We remark that if  $k = r$ , such a result would guarantee that the approximation provided by the neural network can be as accurate as the one of the numerical method  $\Psi_X^{\delta t}$  directly applied to the exact vector field  $X$ . We now characterise the space  $\mathcal{F}$  so that it can exactly represent  $X$ , i.e. make zero the quantity above. However, in practice, this will never be obtained, and the derivation we have presented can quantify the distance of the obtained approximation from the truth.

**3.2. Characterisation of the functional space.** We conclude this section by presenting a functional space  $\mathcal{F}$  that satisfies the two following properties:

- (1) Its elements are functions with a structure which resembles common neural networks.
- (2) Any functions of the form  $X$ , as described in (11), are included in  $\mathcal{F}$  for finite difference operators of first or second-order accuracy.

**3.2.1. Convolutional layers as finite differences.** The finite difference method is a well-known numerical technique to approximate the derivatives of a sufficiently regular function through its evaluation at specific grid points (see, e.g., [44, 54]). The space-time approximation problem introduced in equation (2) of section 2 prevents us from working directly with a smooth function  $u$ . Indeed, what is available is just the sampling of an unknown function  $u$  at specific grid points of a uniform grid on the domain  $[0, 1]^2$ . As a consequence, we are limited in the possibility of choosing the points where we evaluate  $u$  in order to approximate its derivatives. These function evaluations are stored in a matrix that we denote with  $U \in \mathbb{R}^{p \times p}$ . Many techniques have been developed in the image analysis community to identify and locate image edges. These techniques are often based on the interaction between finite differences approximations of derivatives and discrete convolutions (see, e.g., [42, 53]). In this subsection, we briefly present the connection between these two operators. We refer to [17, 37] for a more general derivation that extends to higher-order derivatives.

The discrete convolution operation is the foundation of many successful machine learning algorithms, particularly for approximation tasks involving images. In this work, we focus on ‘same’ convolutions (see, e.g., [22, 28]), i.e. convolution operations that do not change the dimension of the input. We focus on  $3 \times 3$  convolutional filters, however everything we do can be extended to larger convolutional filters. In order to get ‘same’ convolutions, the input matrix has to be padded compatibly with the application of interest. More precisely, the padding strategy in our setting should relate to how the solution of the PDE  $u$  is expected to behave outside the domain  $[0, 1]^2$ , which depends on the boundary conditions. We now report the case of homogeneous Dirichlet boundary conditions ( $U_D$ ) and periodic boundary conditions ( $U_P$ ), which are those considered in the numerical experiments. We report these examples for the specific situation  $U \in \mathbb{R}^{3 \times 3}$ , i.e.

$p = 3$  where we may write

$$U_D = \begin{pmatrix} 0 & 0 & 0 & 0 & 0 \\ 0 & u_{11} & u_{12} & u_{13} & 0 \\ 0 & u_{21} & u_{22} & u_{23} & 0 \\ 0 & u_{31} & u_{32} & u_{33} & 0 \\ 0 & 0 & 0 & 0 & 0 \end{pmatrix} \quad U_P = \begin{pmatrix} u_{33} & u_{31} & u_{32} & u_{33} & u_{31} \\ u_{13} & u_{11} & u_{12} & u_{13} & u_{11} \\ u_{23} & u_{21} & u_{22} & u_{23} & u_{21} \\ u_{33} & u_{31} & u_{32} & u_{33} & u_{31} \\ u_{13} & u_{11} & u_{12} & u_{13} & u_{11} \end{pmatrix}.$$

In general, regardless the value of  $p$ , for  $3 \times 3$  ‘same’ convolutions one has to add two rows and two columns around the matrix  $U$ . The convolution operation  $K * U$  defined by a  $3 \times 3$  kernel, and is a linear map obtained by placing the kernel  $K$  on all the contiguous  $3 \times 3$  submatrices of  $U_D$  or  $U_P$ . In particular, one chooses  $U_D$  in case of zero-padded convolution and  $U_P$  for periodically padded. When the filter is placed over a submatrix, the dot product of the two matrices is computed, and its value will be one entry of the result. We show this procedure in the following example:

$$U_P = \begin{pmatrix} u_{33} & u_{31} & u_{32} & u_{33} & u_{31} \\ u_{13} & u_{11} & u_{12} & u_{13} & u_{11} \\ u_{23} & u_{21} & u_{22} & u_{23} & u_{21} \\ u_{33} & u_{31} & u_{32} & u_{33} & u_{31} \\ u_{13} & u_{11} & u_{12} & u_{13} & u_{11} \end{pmatrix} \\ \Rightarrow R_{11} = \text{vec} \left( \begin{bmatrix} u_{33} & u_{31} & u_{32} \\ u_{13} & u_{11} & u_{12} \\ u_{23} & u_{21} & u_{22} \end{bmatrix} \right)^T \text{vec}(K),$$

where  $R = K * U_P$ , and  $\text{vec}(A)$  is the matrix  $A$  reshaped into a vector. This operation is local as it considers interactions only of the entries of  $3 \times 3$  submatrices.

The same locality property holds for the finite difference operators, which are discrete approximations of the derivatives of a function provided its values at some points in a grid. For example, given a function  $f : [0, 1]^2 \rightarrow \mathbb{R}$  that is three times differentiable in the first component, through Taylor expansions one may verify that

$$\partial_x f(x, y) = \frac{f(x + \delta x, y) - f(x - \delta x, y)}{2\delta x} + \mathcal{O}(\delta x^2).$$

For the PDE (8), if the solution  $u$  is regular enough with respect to  $(x, y)$  we can find a matrix  $K \in \mathbb{R}^{3 \times 3}$  such that

$$\partial_\alpha u(t, x, y) = \sum_{i=-1}^1 \sum_{j=-1}^1 K_{2+i, 2+j} u(t, x + i\delta x, y + j\delta x) + \mathcal{O}(\delta x^2), \quad \alpha \in \mathbb{N}^2, |\alpha| \leq 2,$$

as presented, for example, in [54]. Similarly to image convolutions, in the case of finite differences the function  $u$  needs to be extended outside of the domain due to the boundary conditions. Defining the matrix  $U \in \mathbb{R}^{p \times p}$  (with  $U_{ij} = u(t, x_i, y_j)$ ), there exists some  $K \in \mathbb{R}^{3 \times 3}$  whose action on  $U$  via convolution (i.e.,  $R = K * U$ ) yields

$$R_{ij} = \partial_\alpha u(t, x_i, y_j) + \mathcal{O}(\delta x^2).$$

That is to say, it is possible to express up to second order accuracy any partial derivative of second order or lower. *Consequently, one may observe that (11) can be a second order accurate spatial discretisation of the semi-discretisation of the PDE (8).* An explicit example is the well-known 5-point formula (see [1, Formula 25.3.30]) for approximating the Laplace operator, which is defined as

$$\frac{1}{\delta x^2} \begin{bmatrix} 0 & 1 & 0 \\ 1 & -4 & 1 \\ 0 & 1 & 0 \end{bmatrix} * U = \Delta u(t, x_i, y_j) + \mathcal{O}(\delta x^2).$$

The convolution operator can be extended from matrices to higher-order tensors. In the next subsection, extending it to third-order tensors will be fundamental. For this reason, we now describe how to compute such convolutions. Let  $\mathbf{U} \in \mathbb{R}^{\text{inp} \times p \times p}$  be a generic third-order tensor and  $\mathbf{K} \in \mathbb{R}^{\text{out} \times \text{inp} \times p \times p}$  a fourth-order

tensor representing the set of filters defining the convolution operation. We denote with  $\mathbf{R} \in \mathbb{R}^{\text{out} \times p \times p}$  the result of the convolution operation  $\mathbf{K} * U = \mathbf{R}$ . The components of  $\mathbf{R}$  can be characterised as

$$\mathbf{R}[i] = \sum_{j=1}^{\text{inp}} \mathbf{K}[i, j] * U[j] \in \mathbb{R}^{p \times p}, \quad i = 1, \dots, \text{out},$$

where we recall that

$$\mathbf{K}[i, j] \in \mathbb{R}^{3 \times 3}, \quad i = 1, \dots, \text{out}, j = 1, \dots, \text{inp}.$$

3.2.2. *Definition of the functional space.* Generally, neural networks have the compositional structure

$$\begin{aligned} U^\ell &= T_\ell(U^{\ell-1}), \quad \ell = 1, \dots, L \\ U^0 &= \bar{U} \end{aligned}$$

for some input matrix  $\bar{U}$ , where  $T_\ell$  is obtained by combining non-linear activation functions  $\sigma_\ell : \mathbb{R} \rightarrow \mathbb{R}$  and linear maps. We remark that  $\sigma_\ell$  is usually a scalar function applied to every input entry. Often the activation functions adopted in such an architecture are sigmoidal functions such as tanh. Another common option is the rectified linear unit  $\text{ReLU}(x) := \max\{0, x\}$ . Some publications also have considered powers of such a piecewise linear function (see, e.g., [33, 51]). We will use two activation functions in the neural network representing the function  $X$  in (11), namely  $\sigma_1(x) := \text{ReLU}(x)$  and  $\sigma_2(x) := \text{ReLU}(x)^2$ , whose plots are reported in figure 2. The main reason for this choice is the simple relation

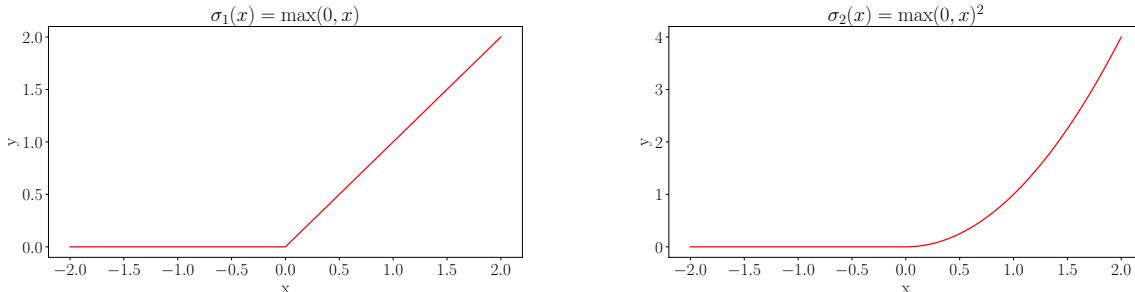


FIGURE 2. Plots of the two activation functions adopted in the architecture

$$x^q = \text{ReLU}(x)^q + (-1)^q \text{ReLU}(-x)^q.$$

This gives, in particular, that polynomials of degree 1 and 2 can be exactly represented by linear functions and the two activation functions  $\sigma_1, \sigma_2$  respectively. These two activation functions are not polynomial. This allows them to be included in networks which can approximate sufficiently regular functions as accurately as desired, see [41]. In this section, however, we want to derive more detailed results than universal approximation theorems can provide. In particular we want theoretical bounds on the number of parameters the networks should have. Before presenting the main theorem, we need to understand how to handle the quadratic non-linearities arising in (11). That is to say, we need to be able to understand product of two matrices through a neural network with the activation functions  $\sigma_1$  and  $\sigma_2$ .

**Lemma 3.1.** For every  $U \in \mathbb{R}^{p \times p}$ ,  $D_1, D_2 \in \mathbb{R}^{3 \times 3}$ , there exist  $\mathbf{M}_1 \in \mathbb{R}^{6 \times 1 \times 3 \times 3}$  and  $\mathbf{M}_2^{1 \times 6 \times 3 \times 3}$ , such that

$$(D_1 * U) \odot (D_2 * U) = \mathbf{M}_2 * \sigma_2(\mathbf{M}_1 * U). \quad (18)$$

We remark that, as in the PyTorch library [40], for the weights of convolutional layers we use the convention  $\mathbf{C} \in \mathbb{R}^{\text{out} \times \text{inp} \times k \times k}$  where inp and out are the number of input and output channels, while  $k$  is the size of the convolutional filter. Before proving this lemma we recall that, as introduced in (5) and (6), we use indices to access the components of third and fourth-order tensors. Additionally, we introduce the notation

$$\mathcal{S}(U) := \sigma_2(U) + \sigma_2(-U) = U \odot U = \mathbf{L}_2 * \sigma_2(\mathbf{L}_1 * U) \quad (19)$$

which makes the proof more compact. For clarity, we explicitly write the tensors  $\mathcal{L}_1, \mathcal{L}_2$  as

$$\begin{aligned}\mathbb{R}^{2 \times 1 \times 3 \times 3} \ni \mathcal{L}_1 &= [[I], [-I]], \\ \mathbb{R}^{1 \times 2 \times 3 \times 3} \ni \mathcal{L}_2 &= [[I, I], \\ & I := \begin{bmatrix} 0 & 0 & 0 \\ 0 & 1 & 0 \\ 0 & 0 & 0 \end{bmatrix},\end{aligned}$$

where remark that  $I$  is the identity convolutional filter, and thus  $I * U = U$ . Hence we have exactly that

$$\begin{aligned}\mathcal{L}_1 * U &= [U, -U] \in \mathbb{R}^{2 \times p \times p}, \\ \sigma_2([U, -U]) &= [\text{ReLU}(U)^2, \text{ReLU}(-U)^2], \\ \mathcal{L}_2 * [\text{ReLU}(U)^2, \text{ReLU}(-U)^2] &= \text{ReLU}(U)^2 + \text{ReLU}(-U)^2 = U \odot U.\end{aligned}$$

*Proof of Lemma 3.1.* We start from the polarization identity  $\frac{1}{2}[(x+y)^2 - x^2 - y^2] = xy$ . Thus, thanks to (19) we know that

$$\begin{aligned}2(D_1 * U) \odot (D_2 * U) &= \mathcal{S}(D_1 * U + D_2 * U) - \mathcal{S}(D_1 * U) - \mathcal{S}(D_2 * U) \\ &= \mathcal{S}((D_1 + D_2) * U) - \mathcal{S}(D_1 * U) - \mathcal{S}(D_2 * U).\end{aligned}$$

We can introduce  $\mathcal{M}_1$  and  $\mathcal{M}_2$  explicitly as

$$\begin{aligned}\mathcal{M}_1[1, 1] &= -\mathcal{M}_1[2, 1] = D_1 + D_2, \\ \mathcal{M}_1[3, 1] &= -\mathcal{M}_1[4, 1] = D_1, \\ \mathcal{M}_1[5, 1] &= -\mathcal{M}_1[6, 1] = D_2, \\ \mathcal{M}_2[1, 1] &= \mathcal{M}_2[1, 2] = \frac{1}{2}I, \\ \mathcal{M}_2[1, 3] &= \mathcal{M}_2[1, 4] = \mathcal{M}_2[1, 5] = \mathcal{M}_2[1, 6] = -\frac{1}{2}I\end{aligned}$$

so that for a generic tensor  $\mathbf{V} \in \mathbb{R}^{6 \times p \times p}$

$$\mathcal{M}_2 * \mathbf{V} = \frac{1}{2}(\mathbf{V}[1] + \mathbf{V}[2]) - \frac{1}{2} \sum_{i=3}^6 \mathbf{V}[i] \in \mathbb{R}^{p \times p},$$

and choosing

$$\mathbf{V} := \sigma_2(\mathcal{M}_1 * U) = \sigma_2([(D_1 + D_2) * U, -(D_1 + D_2) * U, D_1 * U, -D_1 * U, D_2 * U, -D_2 * U]),$$

we may conclude.  $\square$

We are now ready to state and prove the main theorem of this section, where an explicit parametric function  $F_\theta$  is shown to be able to represent  $X$  as in (11).

**Theorem 3.2.** Let  $U \in \mathbb{R}^{p \times p}$  and

$$X(U) = L * U + \sum_{i=1}^n \beta_i (D_{2i-1} * U) \odot (D_{2i} * U) \in \mathbb{R}^{p \times p},$$

for  $L, D_1, D_2, \dots, D_{2n} \in \mathbb{R}^{3 \times 3}$ , where  $n$  represents the number of quadratic interactions. Further let  $F_\theta$  be the parametric map defined by

$$T_1(U) = \mathcal{A}_2 * \sigma_1(\mathcal{A}_1 * U) \in \mathbb{R}^{2n+1 \times p \times p}, U \in \mathbb{R}^{p \times p} \quad (20)$$

$$T_2(\mathbf{V}) = \mathcal{B}_2 * \sigma_2(\mathcal{B}_1 * \mathbf{V}) \in \mathbb{R}^{p \times p}, \mathbf{V} \in \mathbb{R}^{2n+1 \times p \times p} \quad (21)$$

$$F_\theta(U) = \mathcal{C} * T_1(U) + T_2(T_1(U)) \in \mathbb{R}^{p \times p}, U \in \mathbb{R}^{p \times p}. \quad (22)$$

Then,  $F_\theta$  can represent  $X$  for suitably chosen parameters

$$\begin{aligned}\mathcal{A}_1 &\in \mathbb{R}^{(4n+2) \times 1 \times 3 \times 3}, \\ \mathcal{A}_2 &\in \mathbb{R}^{(2n+1) \times (4n+2) \times 3 \times 3}, \\ \mathcal{B}_1 &\in \mathbb{R}^{6n \times (2n+1) \times 3 \times 3}, \\ \mathcal{B}_2 &\in \mathbb{R}^{1 \times 6n \times 3 \times 3}, \\ \mathcal{C} &\in \mathbb{R}^{1 \times (2n+1) \times 3 \times 3}.\end{aligned}$$

*Proof.* The proof is constructive since we report the exact expression of a family of weights that achieves the desired goal. We only specify the parts of the convolutional filters that are non-zero. We first define  $\mathcal{A}_1$  so that

$$\mathcal{A}_1[2i-1, 1] = -\mathcal{A}_1[2i, 1] = D_i, \quad i = 1, \dots, 2n, \quad \mathcal{A}_1[4n+1, 1] = -\mathcal{A}_1[4n+2, 1] = L.$$

Since

$$\sigma_1(P * U) - \sigma_1(-P * U) = P * U, \quad P \in \{D_1, \dots, D_{2n}, L\},$$

we define

$$\mathcal{A}_2[i, 2i-1] = -\mathcal{A}_2[i, 2i] = I, \quad i = 1, \dots, 2n+1.$$

This choice allows getting

$$T_1(U) = [D_1 * U, \dots, D_{2n} * U, L * U] \in \mathbb{R}^{2n+1 \times p \times p}.$$

The convolutional filter  $\mathcal{C}$  needs then just to have  $\mathcal{C}[1, 2n+1] = I$ .

Based on what we have proven in lemma 3.1, we need 6 convolutional filters to represent each interaction of the type  $(D_{2i-1} * U) \odot (D_{2i} * U)$ . Let  $\mathbf{V} \in \mathbb{R}^{2n+1 \times p \times p}$  be a generic tensor that we use to show how  $\mathcal{B}_1$  acts by convolution. We set  $\mathcal{B}_1$  as

$$\begin{aligned}\mathcal{B}_1[6i-5, 2i-1] &= \mathcal{B}_1[6i-5, 2i] = I \implies (\mathcal{B}_1 * \mathbf{V})[6i-5] = \mathbf{V}[2i-1] + \mathbf{V}[2i] \\ \mathcal{B}_1[6i-4, 2i-1] &= \mathcal{B}_1[6i-4, 2i] = -I \implies (\mathcal{B}_1 * \mathbf{V})[6i-4] = -(\mathbf{V}[2i-1] + \mathbf{V}[2i]) \\ \mathcal{B}_1[6i-3, 2i-1] &= -\mathcal{B}_1[6i-2, 2i-1] = \mathcal{B}_1[6i-1, 2i] = -\mathcal{B}_1[6i, 2i] = I,\end{aligned}$$

for  $i = 1, \dots, n$ . This definition gives

$$\begin{aligned}(\mathcal{B}_1 * \mathbf{V})[6i-5 : 6i] &= [(\mathbf{V}[2i-1] + \mathbf{V}[2i]), -(\mathbf{V}[2i-1] + \mathbf{V}[2i]), \\ &\quad \mathbf{V}[2i-1], -\mathbf{V}[2i-1], \mathbf{V}[2i], -\mathbf{V}[2i]].\end{aligned}$$

Here with the notation  $(\mathcal{B}_1 * \mathbf{V})[6i-5 : 6i]$  we refer to the third order tensor

$$[(\mathcal{B}_1 * \mathbf{V})[6i-5], \dots, (\mathcal{B}_1 * \mathbf{V})[6i]] \in \mathbb{R}^{6 \times p \times p}.$$

We can finally define  $\mathcal{B}_2$  as done for  $\mathcal{M}_2$  in the proof of lemma 3.1 as

$$\mathcal{B}_2[1, 6i-5 : 6i] = \frac{\beta_i}{2} [I, I, -I, -I, -I, -I], \quad i = 1, \dots, n$$

so that we get

$$T_2(T_1(U)) = \sum_{i=1}^n \beta_i (D_{2i-1} * U) \odot (D_{2i} * U)$$

concluding the proof.  $\square$

We remark that, apart from the weights involved in  $T_1$ , the weights can be reduced to scalar multiples of the identity filter  $I$ , and hence could also be realised by  $1 \times 1$  convolutions. The choice of the architecture in  $F_\theta$  is not limited to representing only functions with the same structure as  $X$ , and this is the primary motivation behind the choice of not explicitly defining  $F_\theta$  as

$$F_\theta(U) = L * U + \sum_{i=1}^n \beta_i (D_{2i-1} * U) \odot (D_{2i} * U).$$

Indeed, it is generally hard to know if some temporal observations come from the discretisation of a PDE. It is essential that the model we use to approximate such dynamics is as general as possible. We note that any

functional space  $\mathcal{F}$  that contains parametric functions as those in theorem 3.2 is able to represent  $X$ . That is to say many overparametrised networks can be used while maintaining the theoretical guarantees.

We conclude the section with a result which combines results throughout this section and provides the central insight of this theoretical derivation. Indeed, we have constructed a set of parametric functions  $\mathcal{F}$  that allows us to exactly represent the vector fields obtained by semi-discretising PDEs of the form (8). Now, by combining the error splitting in (15) with this approximation bounds for the neural network, we observe the following corollary.

**Corollary 3.3.** Let  $\Psi^{\delta t}$  be a numerical method of order  $r$ . Let

$$\mathcal{S} = \{(U^0, U^1, \dots, U^M)\}$$

be a sequence of snapshots obtained on a regular mesh of  $\Omega = [0, 1]^2$  and with time-step  $\delta t$ , for the PDE (8). Further, assume the measure error  $\varepsilon$  is either zero or of order equal to or higher than  $r$  in time and 2 in space. Then the sequence

$$\hat{U}^{j+1} = \Psi_{F_\theta}^{\delta t}(\hat{U}^j), \quad \hat{U}^0 = U^0, \quad j = 0, \dots, M-1$$

can provide an approximation of  $\mathcal{S}$  accurate to order 2 in space and  $r$  in time if  $F_\theta$  is defined as in Theorem 3.2.

*Proof.* The proof immediately follows by combining the error splitting in (15), the bound on the time-stepper in (16), (17), and theorem 3.2. Indeed, one can get

$$\begin{aligned} \|U^{j+1} - \Psi_{F_\theta}^{\delta t}(U^j)\| &\leq \mathcal{O}(\delta x^2) + \mathcal{O}(\delta t^{r+1}) + \|\varepsilon^{j+1}\| + \|\Psi_X^{\delta t}(U^j) - \Psi_{F_\theta}^{\delta t}(U^j)\| \\ &= \mathcal{O}(\delta x^2) + \mathcal{O}(\delta t^{r+1}) + \|\varepsilon^{j+1}\| \end{aligned}$$

since there exists a  $\theta$  such that  $F_\theta = X$ . □

This corollary guarantees that it is possible to get approximations of the PDE solutions that are second-order accurate in space and  $r$  in time, with networks having a number of parameters growing linearly with the quadratic interactions in the PDE. Furthermore, if one allows for larger convolutional filters, obtaining more accurate finite difference discretisations and extending this result is possible, but beyond the scope of this work. This result can be specialised to the case of linear PDEs. In that case, one could prove that a more straightforward and standard parametric function  $F_\theta$  can be used to represent  $X$  exactly. This function is of the form

$$F_\theta(U) = \mathcal{L}_2 * \text{ReLU}(\mathcal{L}_1 * U).$$

#### 4. NUMERICAL EXPERIMENTS

In this section, we report numerical experiments to support the network architecture introduced in section 3. All neural networks are implemented with the PyTorch library [40] and are trained with an Adam optimiser. Our implementation can be found in [30]. We consider the three following problems:

- (1) linear advection equation,  $\partial_t u = \mathbf{b} \cdot \nabla u = \partial_x u + \partial_y u$ , with doubly periodic spatial boundary conditions,
- (2) heat equation,  $\partial_t u = \alpha \Delta u = \alpha(\partial_{xx} u + \partial_{yy} u)$ , with zero Dirichlet spatial boundary conditions, and
- (3) Fisher equation,  $\partial_t u = \alpha \Delta u + u(1 - u)$ , with zero Dirichlet spatial boundary conditions.

We remark that to reduce the bias introduced by our data-generation technique, we have not used finite difference method to generate the training data. Indeed, we obtain the space-time observations from finite element simulations as described in appendix A. We note that these simulations yield a local truncation error of  $\mathcal{O}(\delta t^3 + \delta x^2)$  allowing us to quantify our measurement error  $\|\varepsilon^j\|$  within this section.

In subsection 4.1, we consider linear advection and compare the results obtained with two networks. These are parametrised in the same way but trained independently with either a norm-preserving projection integrator or explicit Euler. In subsection 4.2, we move on to deal with the dissipative dynamics of the heat equation, where  $\|U^{j+1}\| \leq \|U^j\|$ . Since using explicit Euler does not lead to unstable or inaccurate predictions in our experiments, we only present the results with a network trained with that method. We remark that to obtain dissipative neural networks, one can either add a regularisation term promoting the 1-Lipschitz behaviour of the network (see [25, 43]) or enforce it by construction (see [11, 23]). Finally, in subsection 4.3, we report results for the Fisher equation with the explicit Euler method. Further, to explore

the effectiveness of the network architecture we present, we equip the PDEs with different spatial boundary conditions. The linear advection problem is studied with periodic boundary conditions, while the other two zero Dirichlet ones. This difference leads to a different padding strategy in the convolutional layers, which are periodically padded for linear advection while zero-padded in the other two cases.

Since the results presented in section 3 relate to small networks, we present experiments with networks of moderate size so they are more consistent with the theory. Unfortunately, we could not obtain accurate results with networks of the same size as those presented in the theoretical derivations, so we have embedded them into larger ones. This observation raises the question of whether it is possible to obtain such networks by, for example, designing a more specific optimisation procedure or constraining strategy.

A typical network we present in the following subsections can be described by algorithm 2. Here we specify

---

**Algorithm 2** Evaluation of  $F_\theta(X)$  according to table 1

---

- 1: **Input:**  $X \in \mathbb{R}^{p \times p}$
  - 2:  $L \leftarrow \text{ReLU}(\text{Conv}_1(X)) \in \mathbb{R}^{8 \times p \times p}$
  - 3:  $L \leftarrow \text{ReLU}(\text{Conv}_2(L)) \in \mathbb{R}^{16 \times p \times p}$
  - 4:  $L \leftarrow \text{ReLU}(\text{Conv}_3(L)) \in \mathbb{R}^{8 \times p \times p}$
  - 5:  $L \leftarrow \text{Conv}_4(L) \in \mathbb{R}^{p \times p}$
  - 6:  $Q \leftarrow \text{ReLU}^2(\text{Conv}_5(X)) \in \mathbb{R}^{8 \times p \times p}$
  - 7:  $Q \leftarrow \text{Conv}_6(Q) \in \mathbb{R}^{p \times p}$
  - 8: **return**  $Q + L$
- 

the number of network layers employed to model the approximate vector field and the number of channels the input will have while transformed by these layers. We will summarise this algorithm for compactness through a table, e.g., table 1. Here the number of channels the input has is listed. For example, from line 2 of algorithm 2, we know that  $L = \text{ReLU}(\text{Conv}_1(X))$  has 8 channels and it is computed with the ReLU activation function. This is represented by the value 8 in the second column of the ReLU row in table 1. The reasoning extends similarly to the other entries in the table.

ReLU	1	8	16	8	1
ReLU <sup>2</sup>	1	8	1		

TABLE 1. Simplified view of algorithm 2 listing the involved activation functions and the first dimensionality of the transformed tensor.

To show the accuracy of the trained networks, we report figures representing how three metrics evolve by applying the network to make predictions, iteratively, up to 40 time steps. The metrics are obtained by analysing 30 test initial conditions and are defined as

$$\max\text{E}(j) := \max \left\{ \left| \left( \mathcal{N}_\theta^j(U_i^0) - U_i^j \right)_{hk} \right| : i = 1, \dots, 30, (h, k) \in \{1, \dots, p\}^2 \right\}, \quad (23)$$

$$\text{mse}(j) := \frac{1}{30} \sum_{i=1}^{30} \left( \frac{1}{p^2} \|\mathcal{N}_\theta^j(U_i^0) - U_i^j\|^2 \right), \quad (24)$$

$$\text{rE}(j) := \frac{1}{30} \sum_{i=1}^{30} \left( \frac{\|\mathcal{N}_\theta^j(U_i^0) - U_i^j\|}{\|U_i^j\|} \right), \quad (25)$$

$$\mathcal{N}_\theta^j := \underbrace{\mathcal{N}_\theta \circ \dots \circ \mathcal{N}_\theta}_{j \text{ times}}, \quad j = 1, \dots, 40. \quad (26)$$

We refer to (23) as maximum absolute error, to (24) as mean squared error (MSE), and to (25) as average relative error. All the experiments we report are conducted with  $p = 100$ , i.e., with matrices of size  $100 \times 100$ .

To train the networks we always optimise the function

$$\text{Loss}(\mathcal{N}_\theta, \mathbf{B}, M) := \frac{1}{b \cdot M} \sum_{i=1}^b \sum_{j=1}^M \left\| \mathcal{N}_\theta^j(U_i^0) - U_i^j \right\|^2.$$

We adopt a training procedure which, as described in algorithm 3, pre-trains the network on shorter sequences of snapshots decreasing the learning rate as we increase the length of the sequence,  $M$ , in the training set. In all the experiments,  $b = 32$  is the batch size where  $\mathcal{B}$  denotes one training batch

---

**Algorithm 3** Training procedure

---

```

1: Initialise  $\mathcal{N}_\theta^i$ 
2: Epochs  $\leftarrow 100$ 
3:  $\ell \leftarrow 10^{-2}$  ▷ Set the starting learning rate
4: for  $M \in [3, 4, 5]$  do
5:    $\text{lr} \leftarrow \ell$ 
6:   for  $e < \text{Epochs}$  do
7:     for  $\mathcal{B} \in \text{Batches}$  do
8:       One optimisation step of  $L_\theta(\mathcal{N}_\theta^i, \mathcal{B}, M)$ 
9:     end for
10:    if  $e$  is divisible by 30 then
11:       $\text{lr} \leftarrow \text{lr}/10$  ▷ Learning rate scheduler
12:    end if
13:  end for
14:   $\ell \leftarrow \ell/5$  ▷ Now we add one time step, but we do smaller optimisation steps
15: end for

```

---

$$\mathcal{B} = [\mathbf{U}_1, \dots, \mathbf{U}_b] \in \mathbb{R}^{b \times M \times p \times p},$$

$$\mathbf{U}_i = [U_i^0, U_i^1, \dots, U_i^M] \in \mathbb{R}^{M \times p \times p},$$

and  $M$  is the number of time steps over which we train the network.

**4.1. Linear advection equation.** The linear advection experiments are based on the network architecture reported in table 2. We remark that this PDE is linear, thus it would be possible to limit the parametrisation of the vector field to

$$F_\theta(U) = \mathcal{A}_2 * \text{ReLU}(\mathcal{A}_1 * U), \quad \mathcal{A}_1 \in \mathbb{R}^{2 \times 1 \times 3 \times 3}, \quad \mathcal{A}_2 \in \mathbb{R}^{1 \times 2 \times 1 \times 1}. \quad (27)$$

In practice, we do not get good performance using such a small network and hence we work with the one

ReLU	1	8	16	16	8	1
ReLU <sup>2</sup>	1	8	1			

TABLE 2. Network architecture for the linear advection problem. In this experiment, we assume periodic boundary conditions, and hence all the convolutional layers have circular/periodic padding. Including the bias vectors, this network has 4952 parameters.

represented in table 2. Using similar derivations to section 3, one can show it is possible to represent the map (27) using the network structure described in table 2. The main idea in such derivation is that

$$U = \mathcal{A}_2 * \text{ReLU}(\mathcal{A}_1 * U) = \text{ReLU}(U) - \text{ReLU}(-U) \quad (28)$$

$$\implies U = \mathcal{C}_2 * \text{ReLU}(\mathcal{C}_1 * \mathcal{A}_2 * \text{ReLU}(\mathcal{A}_1 * U)) \quad (29)$$

for suitably chosen  $\mathcal{C}_1$  and  $\mathcal{C}_2$ .

We now analyse the results obtained training the network with two numerical methods that are, as anticipated in section 2,

$$\Psi_{1, F_\theta}^{\delta t} = \varphi_{1, F_\theta}^{\delta t/2} \circ \varphi_{1, F_\theta}^{\delta t/2}, \quad \varphi_{1, F_\theta}^{\delta t'}(U) := U + \delta t' F_\theta(U) \quad (30)$$

$$\Psi_{2, F_\theta}^{\delta t} = \varphi_{2, F_\theta}^{\delta t/2} \circ \varphi_{2, F_\theta}^{\delta t/2}, \quad \varphi_{2, F_\theta}^{\delta t'}(U) := n_{\delta t'}(U) \varphi_{1, F_\theta}^{\delta t'}(U), \quad \text{with } n_{\delta t'}(U) = \frac{\|U\|}{\|\varphi_{1, F_\theta}^{\delta t'}(U)\|}. \quad (31)$$



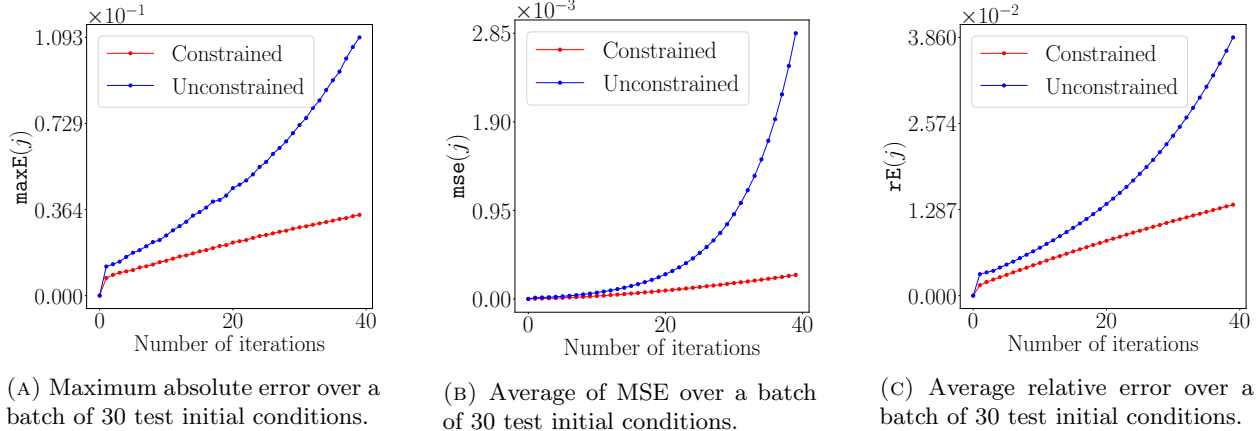


FIGURE 3. Test errors for the linear advection equation

We define two neural networks

$$\mathcal{N}_\theta^i(U) = \Psi_{i,F_\theta}^{\delta t}(U), \quad i = 1, 2,$$

and set  $\delta t = 0.02$ .

Examining figure 3, we observe a significant difference between the accuracy obtained with  $\Psi_{1,F_\theta}^{\delta t}$  and  $\Psi_{2,F_\theta}^{\delta t}$ . In particular, we notice that training the network with a projection method leads to better accuracy of the learned approximation. This result is due to the nature of the data, which come from conservative finite element simulations (see appendix A.1). We remark that the average relative error of 1% after 40 iterates is of the same order as the one we will see later for the Fisher equation, in section 4.3. The results could be improved by considering networks with more parameters or adopting multi-resolution approaches (see [3,38]). However, the purpose of the experiments we report in this section is to show the practical value of the models analysed in the theoretical part of the paper. Thus, our constraint has been working with as small as possible networks while still providing qualitatively accurate predictions of the dynamics.

**4.2. Heat equation.** For the heat equation, we consider a smaller network of 2600 parameters, as represented in table 3, that experimentally proves to be expressive enough. In this case, we train the network only

ReLU	1	8	16	8	1
ReLU <sup>2</sup>	1	8	1		

TABLE 3. Network architecture for the heat equation. For this problem, we assume homogeneous Dirichlet boundary conditions, and hence the convolutional layers are defined with zero-padding.

with explicit Euler, but this time with 3 substeps. The time step is imposed following the CFL condition<sup>1</sup> and is

$$\delta t = 0.24 \cdot \frac{\delta x^2}{\alpha} \approx 2.445 \cdot 10^{-3}.$$

We report the results of this experiment in figure 4. The accuracy of the predictions for this problem is considerably better than the one for the other two equations. This result is due to the linearity of the equation but also to the boundary conditions that characterise this dataset, and the dissipative nature of the dynamics. Indeed, linear advection is linear too, but the periodic behaviour proved to be more difficult to reproduce by the neural network. The effects of boundary conditions and how CNNs produce artefacts at the boundary require further study. We refer to [3] for further investigations.

<sup>1</sup>The details on the values of the diffusivity constant  $\alpha$  can be found in appendix A.1

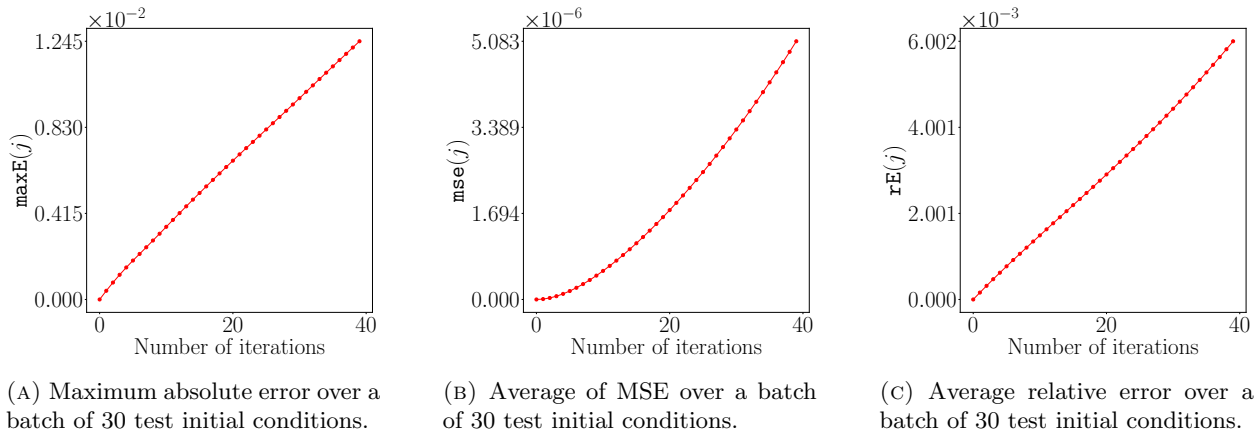


FIGURE 4. Test errors for the heat equation

**4.3. Fisher equation.** For the Fisher equation, which is non-linear, we consider the architecture in table 4. We highlight that the non-linearity appearing in the PDE has  $n = 1$  quadratic term (see theorem 3.2).

ReLU	1	8	16	16	8	1
ReLU <sup>2</sup>	1	16	1			

TABLE 4. Network architecture for the Fisher equation. In this experiment, we assume homogeneous Dirichlet boundary conditions, and hence all the convolutional layers have zero-padding. Including the bias vectors, this network has 5104 parameters.

For this reason, the theoretical derivations in section 3 guarantee that our network can approximate well such a PDE, as long as the number of channels in the ReLU<sup>2</sup> layer is more than 6. The dynamics of this system is more complicated than those of the heat equation. This observation is evident in the results of the numerical experiments and the procedure that allowed us to get them. As presented in appendix A.3, we generate the initial conditions to train and test the network as for the heat equation, and the time step  $\delta t$  has the same value. To obtain the results in figure 5 we selected only the training and test initial conditions for which  $\|U^0\| > 10$ . The value 10 is chosen to obtain a more uniform set of norms in the dataset. This change is due to the low frequency of the initial conditions with small norms that we obtained through the random data generation. The substeps in the numerical method defining the network are 3, as for the heat equation. Overall, the numerical results we present in figure 5 align with those we get for the linear advection problem. In particular, we comment that the relative error after 40 iterations is of the order of 1%, as for the norm-preserving numerical experiment in figure 3.

## 5. CONCLUSION AND FURTHER WORK

This manuscript presents the benefits of approximating temporal sequences of 2-dimensional spatial observations with neural networks inspired by dynamical systems. After a general introduction to the main ideas, where the approach is defined for generic temporal sequences, the focus has been on PDE space-time observations. In particular, we investigated the representation capabilities of popular network architectures for data related to second-order PDEs with quadratic non-linearity.

Exploiting the connections between finite difference operators and discrete convolution, we have shown that it is sufficient to work with quite small-sized networks, where the size grows linearly in the number of interactions appearing in the unknown model. Moreover, the network we investigated can represent broader classes of sequence data than just PDE solutions.

We have also investigated the imposition of norm preservation experimentally. We plan to extend this study by focusing on other properties like the rank of the matrices/tensors propagated by the network. This work also incorporates norm preservation obtained with projection methods, which are generally quite

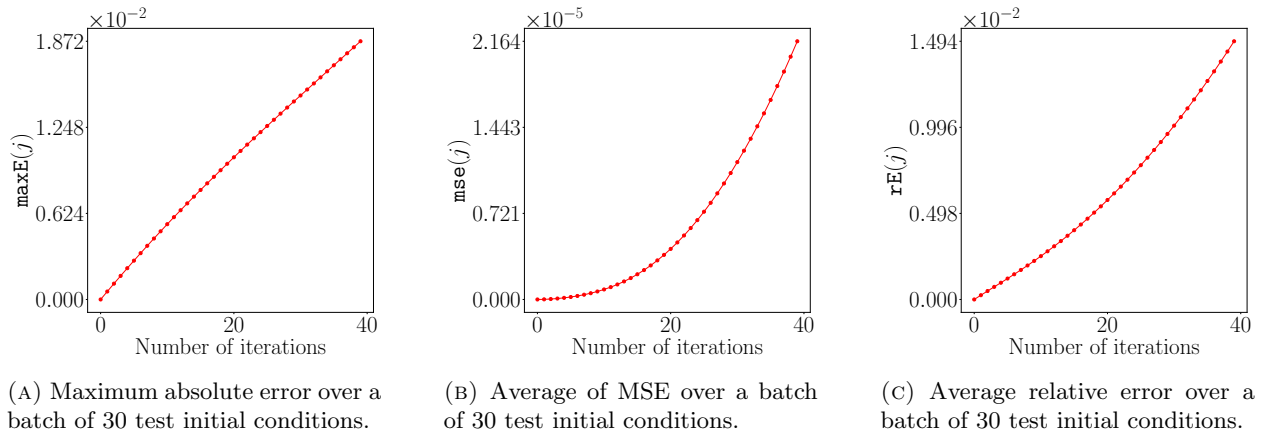


FIGURE 5. Test errors for the Fisher equation

versatile. However, finding the optimal strategy to preserve such structure in practice remains an open question. It would also be interesting to understand the influence of higher-order numerical integrators in the definition and training of neural networks, which we leave for future work.

**Acknowledgements** This work was partially supported by the ERCIM Alain Bensoussan Fellowship Programme (JJ) and by a grant from the Simons Foundation (DM). Funding was also received from the European Union’s Horizon 2020 research and innovation programme under the Marie Skłodowska-Curie grant agreement No 860124, from the Research Council of Norway, and from the Trond Mohn Foundation (EC) and (BO).

## REFERENCES

- [1] Milton Abramowitz, Irene A Stegun, and Robert H Romer. Handbook of mathematical functions with formulas, graphs, and mathematical tables, 1988.
- [2] P-A Absil and Ivan V Oseledets. Low-rank retractions: a survey and new results. *Computational Optimization and Applications*, 62(1):5–29, 2015.
- [3] Antonio Alguacil, Wagner Gonçalves Pinto, Michael Bauerheim, Marc C Jacob, and Stéphane Moreau. Effects of boundary conditions in fully convolutional networks for learning spatio-temporal dynamics. In *Joint European Conference on Machine Learning and Knowledge Discovery in Databases*, pages 102–117. Springer, 2021.
- [4] Jānis Bajārs. Locally-symplectic neural networks for learning volume-preserving dynamics. *Journal of Computational Physics*, page 111911, 2023.
- [5] Yohai Bar-Sinai, Stephan Hoyer, Jason Hickey, and Michael P Brenner. Learning data-driven discretizations for partial differential equations. *Proceedings of the National Academy of Sciences*, 116(31):15344–15349, 2019.
- [6] Alex Bihlo. A generative adversarial network approach to (ensemble) weather prediction. *Neural Networks*, 139:1–16, jul 2021.
- [7] John P Boyd. *Chebyshev and Fourier spectral methods*. Courier Corporation, 2001.
- [8] Susanne Brenner and Ridgway Scott. *The mathematical theory of finite element methods*, volume 15. Springer Science & Business Media, 2007.
- [9] Elena Celledoni, Matthias J Ehrhardt, Christian Etmann, Robert I McLachlan, Brynjulf Owren, Carola-Bibiane Schönlieb, and Ferdia Sherry. Structure-preserving deep learning. *European Journal of Applied Mathematics*, 32(5):888–936, 2021.
- [10] Elena Celledoni, Andrea Leone, Davide Murari, and Brynjulf Owren. Learning hamiltonians of constrained mechanical systems. *Journal of Computational and Applied Mathematics*, 417:114608, 2023.
- [11] Elena Celledoni, Davide Murari, Brynjulf Owren, Carola-Bibiane Schönlieb, and Ferdia Sherry. Dynamical systems’ based neural networks. *arXiv preprint arXiv:2210.02373*, 2022.
- [12] Gianluca Ceruti and Christian Lubich. An unconventional robust integrator for dynamical low-rank approximation. *BIT Numerical Mathematics*, 62(1):23–44, 2022.
- [13] Ricky TQ Chen, Yulia Rubanova, Jesse Bettencourt, and David K Duvenaud. Neural ordinary differential equations. *Advances in neural information processing systems*, 31, 2018.
- [14] Zhengdao Chen, Jianyu Zhang, Martin Arjovsky, and Léon Bottou. Symplectic recurrent neural networks. *arXiv preprint arXiv:1909.13334*, 2019.
- [15] Taco Cohen and Max Welling. Group equivariant convolutional networks. In *International conference on machine learning*, pages 2990–2999. PMLR, 2016.

- [16] Salvatore Cuomo, Vincenzo Schiano Di Cola, Fabio Giampaolo, Gianluigi Rozza, Maziar Raissi, and Francesco Piccialli. Scientific machine learning through physics-informed neural networks: Where we are and what's next. *Journal of Scientific Computing*, 92(3), jul 2022.
- [17] Bin Dong, Qingtang Jiang, and Zuwei Shen. Image restoration: Wavelet frame shrinkage, nonlinear evolution PDEs, and beyond. *Multiscale Modeling & Simulation*, 15(1):606–660, 2017.
- [18] Weinan E. A proposal on machine learning via dynamical systems. *Communications in Mathematics and Statistics*, 1(5):1–11, 2017.
- [19] Leah Edelstein-Keshet. *Mathematical models in biology*. SIAM, 2005.
- [20] Lawrence C. Evans. *Partial differential equations*, volume 19 of *Graduate Studies in Mathematics*. American Mathematical Society, Providence, RI, 1998.
- [21] Stathi Fotiadis, Eduardo Pignatelli, Mario Lino Valencia, Chris Cantwell, Amos Storkey, and Anil A Bharath. Comparing recurrent and convolutional neural networks for predicting wave propagation. *arXiv preprint arXiv:2002.08981*, 2020.
- [22] Ian Goodfellow, Yoshua Bengio, and Aaron Courville. *Deep learning*. MIT press, 2016.
- [23] Henry Gouk, Eibe Frank, Bernhard Pfahringer, and Michael J Cree. Regularisation of neural networks by enforcing lipschitz continuity. *Machine Learning*, 110:393–416, 2021.
- [24] Bartosz A Grzybowski. *Chemistry in motion: reaction-diffusion systems for micro-and nanotechnology*. John Wiley & Sons, 2009.
- [25] Ishaan Gulrajani, Faruk Ahmed, Martin Arjovsky, Vincent Dumoulin, and Aaron C Courville. Improved training of wasserstein gans. *Advances in neural information processing systems*, 30, 2017.
- [26] Eldad Haber and Lars Ruthotto. Stable architectures for deep neural networks. *Inverse problems*, 34(1):014004, 2017.
- [27] Ernst Hairer, Christian Lubich, and Gerhard Wanner. *Geometric Numerical Integration: Structure-Preserving Algorithms for Ordinary Differential Equations*. Springer, 2006.
- [28] Per Christian Hansen, James G Nagy, and Dianne P O'leary. *Deblurring images: matrices, spectra, and filtering*. SIAM, 2006.
- [29] James Jackaman and Davide Murari. Data used in predictions based on pixel data: Insights from PDEs and finite differences. 10.5281/zenodo.7665159, 2023.
- [30] James Jackaman and Davide Murari. Implementation used in 'predictions based on pixel data: Insights from pdes and finite differences. 10.5281/zenodo.7678902, 2023.
- [31] Pengzhan Jin, Zhen Zhang, Aiqing Zhu, Yifa Tang, and George Em Karniadakis. SympNets: Intrinsic structure-preserving symplectic networks for identifying hamiltonian systems. *Neural Networks*, 132:166–179, 2020.
- [32] Emil Kieri and Bart Vandereycken. Projection methods for dynamical low-rank approximation of high-dimensional problems. *Computational Methods in Applied Mathematics*, 19(1):73–92, 2019.
- [33] Jason M Klusowski and Andrew R Barron. Approximation by combinations of ReLU and squared ReLU ridge functions with  $\ell^1$  and  $\ell^0$  controls. *IEEE Transactions on Information Theory*, 64(12):7649–7656, 2018.
- [34] Othmar Koch and Christian Lubich. Dynamical low-rank approximation. *SIAM Journal on Matrix Analysis and Applications*, 29(2):434–454, 2007.
- [35] Tamara G Kolda and Brett W Bader. Tensor decompositions and applications. *SIAM review*, 51(3):455–500, 2009.
- [36] Randall J LeVeque. *Finite difference methods for ordinary and partial differential equations: steady-state and time-dependent problems*. SIAM, 2007.
- [37] Zichao Long, Yiping Lu, and Bin Dong. PDE-Net 2.0: Learning pdes from data with a numeric-symbolic hybrid deep network. *Journal of Computational Physics*, 399:108925, 2019.
- [38] Michael Mathieu, Camille Couprie, and Yann LeCun. Deep multi-scale video prediction beyond mean square error. *arXiv preprint arXiv:1511.05440*, 2015.
- [39] Sergiu Oprea, Pablo Martinez-Gonzalez, Alberto Garcia-Garcia, John Alejandro Castro-Vargas, Sergio Orts-Escolano, Jose Garcia-Rodriguez, and Antonis Argyros. A review on deep learning techniques for video prediction. *IEEE Transactions on Pattern Analysis and Machine Intelligence*, 44(6):2806–2826, 2020.
- [40] Adam Paszke, Sam Gross, Francisco Massa, Adam Lerer, James Bradbury, Gregory Chanan, Trevor Killeen, Zeming Lin, Natalia Gimelshein, Luca Antiga, Alban Desmaison, Andreas Kopf, Edward Yang, Zachary DeVito, Martin Raison, Alykhan Tejani, Sasank Chilamkurthy, Benoit Steiner, Lu Fang, Junjie Bai, and Soumith Chintala. PyTorch: An imperative style, high-performance deep learning library. In *Advances in Neural Information Processing Systems 32*, pages 8024–8035. Curran Associates, Inc., 2019.
- [41] Allan Pinkus. Approximation theory of the MLP model in neural networks. *Acta numerica*, 8:143–195, 1999.
- [42] William K Pratt. *Digital image processing: PIKS Scientific inside*, volume 4. Wiley Online Library, 2007.
- [43] Guo-Jun Qi. Loss-sensitive generative adversarial networks on lipschitz densities. *International Journal of Computer Vision*, 128(5):1118–1140, 2020.
- [44] Alfio Quarteroni, Riccardo Sacco, and Fausto Saleri. *Numerical mathematics*, volume 37. Springer Science & Business Media, 2010.
- [45] M. Raissi, P. Perdikaris, and G.E. Karniadakis. Physics-informed neural networks: A deep learning framework for solving forward and inverse problems involving nonlinear partial differential equations. *Journal of Computational Physics*, 378:686–707, feb 2019.
- [46] Florian Rathgeber, David A. Ham, Lawrence Mitchell, Michael Lange, Fabio Luporini, Andrew T. T. McRae, Gheorghe-Teodor Bercea, Graham R. Markall, and Paul H. J. Kelly. Firedrake: automating the finite element method by composing abstractions. *ACM Trans. Math. Software*, 43(3):Art. 24, 27, 2017.

- [47] Samuel Rudy, Alessandro Alla, Steven L Brunton, and J Nathan Kutz. Data-driven identification of parametric partial differential equations. *SIAM Journal on Applied Dynamical Systems*, 18(2):643–660, 2019.
- [48] Sebastian Scher and Gabriele Messori. Predicting weather forecast uncertainty with machine learning. *Quarterly Journal of the Royal Meteorological Society*, 144(717):2830–2841, oct 2018.
- [49] William E Schiesser. *The numerical method of lines: integration of partial differential equations*. Elsevier, 2012.
- [50] William E Schiesser and Graham W Griffiths. *A compendium of partial differential equation models: method of lines analysis with Matlab*. Cambridge University Press, 2009.
- [51] David So, Wojciech Mańke, Hanxiao Liu, Zihang Dai, Noam Shazeer, and Quoc V Le. Searching for efficient transformers for language modeling. *Advances in Neural Information Processing Systems*, 34:6010–6022, 2021.
- [52] Walter A. Strauss. *Partial differential equations*. John Wiley & Sons, Ltd., Chichester, second edition, 2008. An introduction.
- [53] Richard Szeliski. *Computer vision: algorithms and applications*. Springer Nature, 2022.
- [54] James William Thomas. *Numerical partial differential equations: finite difference methods*, volume 22. Springer Science & Business Media, 2013.
- [55] Geoffrey K Vallis. *Atmospheric and oceanic fluid dynamics*. Cambridge University Press, 2017.
- [56] Rui Wang, Karthik Kashinath, Mustafa Mustafa, Adrian Albert, and Rose Yu. Towards physics-informed deep learning for turbulent flow prediction. In *Proceedings of the 26th ACM SIGKDD International Conference on Knowledge Discovery & Data Mining*, pages 1457–1466, 2020.
- [57] Rui Wang, Robin Walters, and Rose Yu. Incorporating symmetry into deep dynamics models for improved generalization. *arXiv preprint arXiv:2002.03061*, 2020.
- [58] Yunbo Wang, Haixu Wu, Jianjin Zhang, Zhifeng Gao, Jianmin Wang, S Yu Philip, and Mingsheng Long. Predrnn: A recurrent neural network for spatiotemporal predictive learning. *IEEE Transactions on Pattern Analysis and Machine Intelligence*, 45(2):2208–2225, 2022.
- [59] Hao Xu, Haibin Chang, and Dongxiao Zhang. DL-PDE: Deep-learning based data-driven discovery of partial differential equations from discrete and noisy data. *arXiv preprint arXiv:1908.04463*, 2019.
- [60] Aiqing Zhu, Pengzhan Jin, and Yifa Tang. Deep Hamiltonian networks based on symplectic integrators. *arXiv preprint arXiv:2004.13830*, 2020.

## APPENDIX A. DATA GENERATION

Throughout our numerical experiments in section 4 we have relied on finite element discretisations to generate data. This data set can be found in [29]. For completeness, here we will briefly outline the methods used. Throughout, spatially we utilise piece-wise continuous linear Lagrange finite elements which, to a reasonable extent, respect the PDE dynamics. Crucially, any data which is generated must be interpolated (preferably in a structure preserving manner) as a set of matrices. Recall that the entries of the matrix represent points in two dimensional space with each matrix corresponding to a discrete “snapshot” of the solution in time. With this matrix structure in mind, we choose to mesh our domain with regular quadrilaterals (as opposed to the more typical triangulation) and utilise bi-quadratic basis functions. Indeed, through doing so with linear elements the degrees of freedom of the methods will be represented exactly by the values of the matrix. In particular, we shall write this finite element space as  $\mathbb{V}$  which implicitly depends on the meshing of our domain. Throughout, we fix our matrix dimension to be  $\mathbb{R}^{100 \times 100}$ , which fixes our mesh resolution to be  $p = 100$ , where  $p$  corresponds to the number of subrectangles in both the  $x$  and  $y$  direction. Temporally, we utilise second order implicit time stepping methods, and define the temporal evolution through the time step  $\delta t$ . For ease of implementation, we utilise the finite element library Firedrake [46], and our implementation can be found in [30]. Each simulation is initialised by “random” initial data, which is problem dependent and we describe below.

**A.1. Linear advection.** Let  $u = u(t, x, y)$ , where  $(x, y) \in \Omega := [0, 1]^2$  doubly periodic and  $t \in [0, T]$ . Then, we may express linear advection as

$$\partial_t u = \mathbf{b} \cdot \nabla u, \tag{32}$$

where  $\mathbf{b} \in \mathbb{R}^2$  is some specified constant subject to the initial condition  $u(0, x, y) = u_0$ . To clarify exposition we shall focus on the first time step of the method, which may be easily extrapolated for all time. Let  $U_0$  be given by the interpolation of the initial data  $u_0$  into the finite element space, then the solution at the next time step is given by seeking  $U_1 \in \mathbb{V}$  such that

$$\int_{\Omega} \left( \frac{U_1 - U_0}{\delta t} + \mathbf{b} \cdot \nabla U_{\frac{1}{2}} \right) \phi \, d\mathbf{x} \quad \forall \phi \in \mathbb{V}, \tag{33}$$

where  $U_{\frac{1}{2}} = \frac{1}{2} (U_0 + U_1)$ .

One key property of this method is that it preserves both a discrete mass and momentum. To be more concise the mass  $\int_{\Omega} U_1 \, d\mathbf{x} = \int_{\Omega} U_0 \, d\mathbf{x}$  is constant over time, as can be observed by virtue of the periodic boundary conditions and after choosing  $\phi = 1$ . More importantly, the momentum  $\int_{\Omega} U_1^2 \, d\mathbf{x} = \int_{\Omega} U_0^2 \, d\mathbf{x}$  is conserved, as may be observed after choosing  $\phi = U_{\frac{1}{2}}$ . Conservation of momentum is equivalent to preserving the norm of the underlying matrix.

In section 4.1 our random initial conditions are generated by

$$u_0 = \sin(2\pi\alpha_1(x - x_s)) \cos(2\pi\alpha_2(y - y_s)) + 1, \quad (34)$$

where  $\alpha_i \sim U(\{5, 6, 7, 8\})$  are independently sampled with equal likelihood and  $x_s, y_s \sim U([0, 1])$  are sampled from a unitary uniform distribution. Further, we fix the time step to be  $\delta t = 0.02$  and  $\mathbf{b} = (1, 1)$  throughout the experiments.

**A.2. Heat equation.** Here we utilise the same set up as the heat equation without the assumption of being doubly periodic. That is to say, we let  $u = u(t, x, y)$  where  $(x, y) \in \Omega = [0, 1]^2$  and  $t \in [0, T]$ , be given by

$$u_t = \alpha \Delta u \quad \text{on } \Omega \quad (35)$$

$$u = 0 \quad \text{on } \partial\Omega, \quad (36)$$

where  $\alpha \in \mathbb{R}$  is the dissipation constant, and subject to the initial condition  $u(0, x, y) = u_0$ . To simplify exposition, we directly impose the boundary conditions on the finite element space  $\mathbb{V}$ . That is to say, for all  $v \in \mathbb{V}$ ,  $v|_{\partial\Omega} = 0$ . Letting  $U_0$  be the interpolation of some given randomised initial data into the finite element space  $\mathbb{V}$ , the numerical method is described by seeking  $U_1 \in \mathbb{V}$  such that

$$\int_{\Omega} \left( \frac{U_1 - U_0}{\delta t} \right) \phi + c \nabla U_{\frac{1}{2}} \cdot \nabla \phi \, d\mathbf{x} = 0 \quad \forall \phi \in \mathbb{V}. \quad (37)$$

In section 4.2, we exploit the dissipative behaviour of this equation. Indeed, this numerical method respects the physical rate of dissipation, through choosing  $\phi = U_{\frac{1}{2}}$  we observe

$$\int_{\Omega} U_1^2 \, d\mathbf{x} = \int_{\Omega} U_0^2 - c \int_{\Omega} \nabla U_{\frac{1}{2}}^2 \, d\mathbf{x}, \quad (38)$$

which is consistent with the true rate of dissipation in the heat equation.

In section 4.2 our random initial conditions are generated by

$$u_0 = \beta \sin(k\pi(x - 1)) \sin(k\pi(y - 1)), \quad (39)$$

where  $k \sim U(\{2, 3, 4, 5, 6, 7\})$  is randomly selected and  $\beta \sim \mathcal{N}(1, 0.5)$  is normally distributed with mean 1 and variance 0.5. Further, throughout our experiments we fix  $\delta t = 0.024$  and  $c = 0.01$ .

**A.3. Fisher equation.** Let us consider, through modification of the heat equation, a nonlinear reaction diffusion equation. In particular, let  $u = u(t, x, y)$  solve the reaction diffusion equation

$$u_t = \alpha \Delta u + u(1 - u) \quad \text{on } \Omega \quad (40)$$

$$u = 0 \quad \text{on } \partial\Omega, \quad (41)$$

subject to some (randomised) initial data  $u(0, x, y) = u_0$ . Letting  $U_0$  be given by the interpolation of  $u_0$  into the finite element space, the first step of the method is given by seeking  $U_1 \in \mathbb{V}$  such that

$$\int_{\Omega} \left( \frac{U_1 - U_0}{\delta t} \right) \phi + c \nabla U_{\frac{1}{2}} \cdot \nabla \phi - \left( U_{\frac{1}{2}} + \frac{1}{3} (U_1^2 + U_1 U_0 + U_0^2) \right) \phi \, d\mathbf{x} = 0 \quad \forall \phi \in \mathbb{V}. \quad (42)$$

Note here that the choice of temporal discretisation for the nonlinear term is not unique and we have chosen a second-order accurate temporal discretisation.

In section 4.3, due to similarities in the setup, the random initial conditions generated are the same as for the heat equation. To be more concise, we specify

$$u_0 = \beta \sin(k\pi(x - 1)) \sin(k\pi(y - 1)), \quad (43)$$

where  $k \sim U(\{2, 3, 4, 5, 6, 7\})$  and  $\beta \sim \mathcal{N}(1, 0.5)$ . Additionally, throughout the experiments we maintain  $\delta t = 0.024$  and  $\alpha = 0.01$ .

ELENA CELLEDONI DEPARTMENT OF MATHEMATICAL SCIENCES, NTNU, 7491 TRONDHEIM, NORWAY [elena.celledoni@ntnu.no](mailto:elena.celledoni@ntnu.no)

JAMES JACKAMAN DEPARTMENT OF MATHEMATICAL SCIENCES, NTNU, 7491 TRONDHEIM, NORWAY [james.jackaman@ntnu.no](mailto:james.jackaman@ntnu.no)

DAVIDE MURARI DEPARTMENT OF MATHEMATICAL SCIENCES, NTNU, 7491 TRONDHEIM, NORWAY [davide.murari@ntnu.no](mailto:davide.murari@ntnu.no)

BRYNJULF OWREN DEPARTMENT OF MATHEMATICAL SCIENCES, NTNU, 7491 TRONDHEIM, NORWAY [brynjulf.owren@ntnu.no](mailto:brynjulf.owren@ntnu.no)